Real-Time Tracking of a Bevel-tip Needle with Varying Insertion Depth: Toward Teleoperated MRI-guided Needle Steering*

Reza Seifabadi, Esteban Escobar Gomez, Fereshteh Aalamifar, Gabor Fichtinger, and Iulian Iordachita

Abstract— This study presents one of the enabling technologies for teleoperated bevel-tip needle steering under real-time MRI guidance i.e. capability of tracking the needle with higher accuracy and bandwidth than real-time MRI. Three fibers, each with three Fiber Bragg Gratings (FBG) were embedded into a 0.6 mm inner stylet of a 20G MRI-compatible biopsy needle. The axial force caused by the bevel-tip was considered in the analysis using beam-column theory. Since the insertion depth is varying, the minimum number of sensors and their optimal locations in the fibers were determined such that the tip position error estimation is below 0.5 mm for all insertion depths. A practical and accurate calibration method for the apparatus is presented. The instrumented needle was fabricated to fit in the needle driver unit of a MRI-compatible needle steering robot. The tracking apparatus was calibrated, including compensation for temperature changes in tissue during insertion. Experimental results showed needle tip tracking error below 0.5 mm at different insertion depths. Real-time 3D shape of the needle was visualized in 3D Slicer yielding navigation of the needle in real-time.

I. INTRODUCTION

MRI is the superior imaging modality for visualization of prostate and detection of cancerous tissues. MRI-compatible robots could improve the efficacy of needle placement in prostate biopsy and brachytherapy. We proposed human-operated in-room, master-slave needle steering under real-time MRI guidance to reduce number of patient removals from the scanner while having continuous human supervision in the loop (Fig. 1) [1], [18]. Bevel-tip needle steering is proposed to compensate for the error happening during needle insertion including prostate motion [2] and needle deflection [3]. To enable teleoperated bevel-tip needle steering under continuous MRI guidance, different technologies have to be developed including MRI-compatible haptic devices [4], MRI-compatible force sensors [5], target tracking [6], and needle tracking. This study focuses on needle tracking aspect.

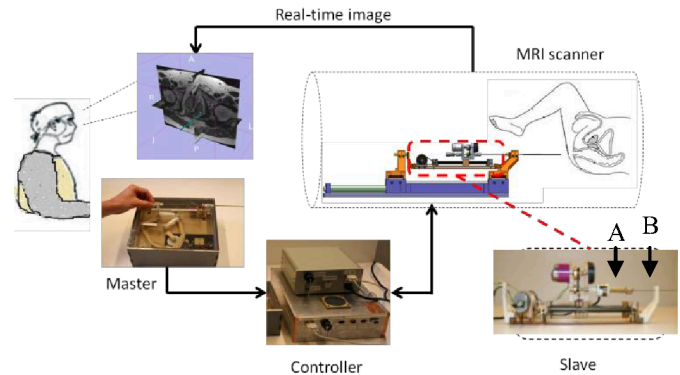A flexible bevel-tip needle bends during insertion due to

Figure 1. Teleoperated needle steering under real-time MRI guidance.

asymmetric lateral forces applied to the bevel-tip. If it is rotated 180 degrees, the bending direction reverses making the needle tip deflect to the opposite direction. One dependency for enabling of this steering technique is providing visual information of the needle tip (and target) on the fly. The immediate solution would be real-time MRI. However, real-time MR imaging has some limitations: 1) needle leaves a large artifact on the image (few mm thick) and it is not straightforward to localize needle shaft within the artifact since it depends on many factors including imaging parameters [7]; 2) real-time imaging involves 500 msec latency in typical scanners, 3) for most of the scanners, it is difficult to interactively control the imaging plane such that the 3D shape of needle can be captured during insertion. In addition, using radio frequency tracking passive coils is not practical as this method requires very small coils to be embedded into the 0.6 mm inner stylet of the needle.

An FBG sensor is a strain gauge consisting of an optic fiber with a short segment of grated mirrors in series allowing a different wavelength to be reflected and collected. As the fiber experiences mechanical or thermal stresses, the distances between these mirrors change, resulting in a shift of the wavelength. This shift in wavelength is proportional to the strain the fiber experiences [8]. By principle, FBG has no interference with MRI magnetic field. Some advantages of FBGs are high accuracy, fast response, robustness, bio-compatibility and sterilizability, making it a good solution for our application.

FBG technology has been previously used for a variety of needle and surgical tool applications. A needle having 3 embedded fibers in 120 degree configuration was proposed for measurement of sub-milli Newton lateral force applied to

R. Seifabadi, E. E. Gomez, F. Aalamifar and I. Iordachita are with Laboratory for Computational Sensing and Robotics (LCSR), The Johns Hopkins University, Baltimore, MD, US.

R. Seifabadi and G. Fichtinger are with Laboratory for Percutaneous surgery (Perk Lab), Queen's University, Kingston, Canada.

Corresponding author: iordachita@jhu.edu

a 25G tool shaft for vitroretinal surgery [9]. A similar idea was used to capture the 3D shape of a diamond-tip 18G needle with fixed length [10]. FBGs have also been used to estimate 3D shape of the catheters and endoscopes in similar fashion [11], [12].

In this study, we embed 3 optical fibers ($\emptyset$ = 125 μm) with constructed FBGs along the inner stylet of a 20G MRI-compatible bevel-tip needle (Fig. 2). We show that minimum 3 FBGs along each fiber are required to render 3D shape of needle for all possible insertion depths i.e. depths in the range of 0 - 110 mm. The optimum locations of FBGs are found by mathematical modeling and computer simulation such that the error in tip estimation is below 0.5 mm for any insertion depth. Beam-column theory is employed in modeling of the needle deflection in order to account for the concentrated lateral and axial forces applied to the bevel-tip. The needle is custom designed to be used at the slave robot needle holder. After prototyping the needle, a simple and practical method for calibration is proposed without requirement of camera and image processing. Accuracy of the system in estimation of the needle tip for different insertion depths are demonstrated with experiments. Real-time 3D visualization of the needle is enabled in 3D Slicer which is a software used in clinical procedures for prostate biopsy and brachytherapy [13]. A video is provided to show this capability.
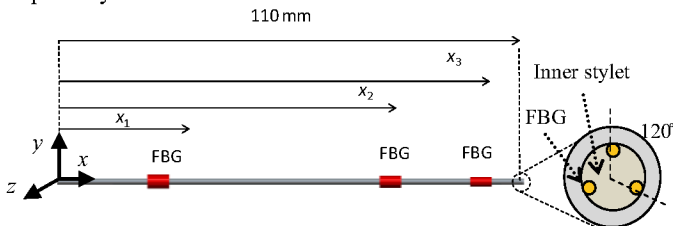

Figure 2. Needle with 3 optical fibers at 120 degree configuration. Each fiber has 3 FBGs at x_1, x_2, and x_3, respectively.

II. DESIGN CONSIDERATIONS

In this study, we aim to track 3D shape of a bevel-tip MRI-compatible biopsy needle in real-time. 20G ($\emptyset$ = 0.9 mm) needle is selected since it is flexible enough for steering purposes and still thick enough for embedding fibers into its inner stylet ($\emptyset$ = 0.6 mm). We considered minimum and maximum insertion depths in transperineal prostate biopsy and brachytherapy to be 20 mm and 100 mm, respectively (most often in the range of 40 - 70 mm). The actual needle is longer considering the slave robot geometry (Fig. 1). However, the length-of-interest i.e. the length to be monitored is 110 mm (extra 10 mm is considered for the distance between the premium and robot).

Target displacement (caused by prostate motion and deformation) increases with insertion depth. In this study, we assume that target displacement does not exceed 10 percent of the insertion depth which means up to 10 mm displacement when the needle is fully inserted (i.e. 100 mm). This is a fairly large displacement in comparison to the average 5.4 mm (1.6 - 11.1 mm) target displacement in transrectal prostate biopsy

reported by Xu [14]. This assumption allows us to use linear beam theory.

We define the maximum tolerable tip estimation error to be 0.5 mm for all insertion depths. This error threshold is considered to be relatively small since the other sources of error (such as prostate motion and errors associated with the robotic system) have larger contributions into the maximum 5 mm tolerable error in prostate biopsy [3]. The technology should be MRI-compatible. To cover most of the deflection scenarios, our method should be able to show the needle shape with at least two inflection points (Fig. 3). This means a minimum 2 FBGs per fiber is required. Lastly, it is desired not to have noticeable latency during needle monitoring.
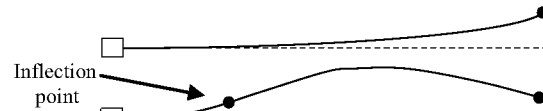

Figure 3. Needle with one and two inflection points. Tip is one of the inflection point.

III. TIP POSITION ESTIMATION

Needle tip position could be defined as $[x, y, z]$ where x is the insertion depth measured by the slave robot encoder, and y and z are lateral deflections. We use polynomial fit to estimate the needle profile. To find y, suppose that the needle is only deflected in x-y plane and the needle profile has $n+1$ inflection points (tip is one of them). This means an n-th order polynomial can be fit to those n inflection points i.e. the second derivative of the profile could be represented by an n-th order polynomial. An n-th order polynomial has $n+1$ unknown ($a_1x^n + a_2x^{n-1} + \cdots + a_{n+1}$). To find these unknowns, one needs to know the second derivative at n different locations along the profile other than the tip (tip gives us the $(n+1)$-th constant). In order to measure the second derivative at the abovementioned n points, we use n FBGs and find the corresponding second derivative from equation (1) [15]:

$$y''(x) = \frac{\varepsilon_{x-y}}{r} \qquad (1)$$

where ε_{x-y} is strain in x-y plane and r is the radius of gyration (= the needle radius). Then, we can solve a set of $n+1$ equations and attain the polynomial's coefficients. After finding the estimated second derivative polynomial, we double integrate and derive the approximate profile of the needle. In the equation, we put $x = l$ where l is insertion depth and find y. We found z in similar way using the set of sensors on the second fiber containing n FBGs located on the x-z plane. The set of n sensors on the third fiber are used for temperature compensation. These three fibers are placed at 120 degree configuration [9] (Fig. 2).

The needle tip accuracy increases with a higher number of sensors along the needle length. However, a higher number of FBGs means higher manufacturing costs and increased susceptibility to fiber damage or malfunction. It also means higher complexity for calibration, and requires higher data processing time through the interrogator and streaming socket protocol, which will slow down real-time visualization of the needle profile and tip location. As a result, it was deemed

necessary to find the minimum number of sensors that would be able to provide an error threshold smaller than 0.5 mm for all depth configurations. As mentioned earlier, a minimum two sensors is required to estimate the shape of the needle in each plane with two inflection points. However, the localization analysis proved that for low insertion depths with only one active sensor, the error noticeably exceeds 0.5 mm. In order to compensate for this, we use three sensors along each fiber as will be discussed next.

For a three sensor case, $y''(x)$ can be approximated as follows:

$$y''(x) = a_y x^3 + b_y x^2 + c_y x + d_y \qquad (2)$$

To find a_y, b_y, c_y, and d_y, we use strain information at x_1, x_2, x_3, from (1), and at the tip (which is 0). Having $y''(x)$ at 4 points, a_y, b_y, c_y, and d_y could be found as follows:

$$\begin{bmatrix} a_y \\ b_y \\ c_y \\ d_y \end{bmatrix} = \begin{bmatrix} x_1^3 & x_1^2 & x_1 & 1 \\ x_2^3 & x_2^2 & x_2 & 1 \\ x_3^3 & x_3^2 & x_3 & 1 \\ L^3 & L^2 & L & 1 \end{bmatrix}^{-1} \begin{bmatrix} y''(x_1) \\ y''(x_2) \\ y''(x_3) \\ 0 \end{bmatrix} \qquad (3)$$

L is the instantaneous length of the needle. If we double integrate equation (2) and apply the boundary conditions, the approximated profile is obtained as follows:

$$y^{app}(x) = \frac{a_y}{20}x^5 + \frac{b_y}{12}x^4 + \frac{c_y}{6}x^3 + \frac{d_y}{2}x^2 \qquad (4)$$

The approximate position of the needle tip then would be $y(L)$. The profile on the x-z plane, $z(x)$ is found in the same manner. In the next section, sensor localization i.e. finding optimum x_1, x_2, and x_3 is discussed in detail.

IV. SENSOR LOCALIZATIONS

The needle tip pose estimation error can be defined as the difference between the approximated and the actual tip position:

$$\text{Error}(x_1, x_2, x_3) = |y^{actual} - y^{app}| \qquad (5)$$

This error is a function of x_1, x_2, and x_3. To minimize this error, the optimum sensor locations should be found for all insertion depths and possible needle profiles. For this reason, we need to generate all possible needle profiles and insertion depths and see what sensor locations make the smallest error among all. The only practical method of searching among that infinite number of possibilities is development of a model for needle deflection. This model gives a mathematical function by which we can measure y^{actual} and y^{app} for any shape and depth and, as a result, determined the proper sensor locations based on Equation (5).

A. Modeling

Fig. 1 shows the needle steering robot. For our application, the utilized free body diagram is as shown in Fig. 4. F_y is the concentrated lateral force at the tip, F_x is the concentrated axial force at the tip due to the bevel-tip, w is the distributed load applied to the needle inside tissue, the factor a is the needle length not inserted into the tissue but still deflected from the loads applied, and L is the instantaneous needle length. Here, we ignore torsion along the needle since we did
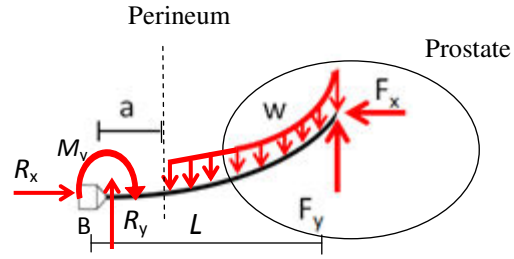

Figure 4. Free body diagram (FBD) for the bevel-tip needle during insertion.

not observe torsional lag between the base and the tip in phantom experiments. Although this FBD might not be the most accurate one, it is still adequate because this approach focuses not on what types of forces are applied but on what needle shapes can be created. As a result, a force configuration that generates a variety of needle shapes with up to two inflection points will allow derivation of mathematical models and optimization.

The needle can be modeled as an Euler-Bernoulli beam since the maximum tip deflection is limited to 10% of the length. We experimentally confirmed this assumption (i.e. the linear relationship between the force and tip deflection) for the 20G needle we used. The Euler-Bernoulli beam's governing differential equation is as follows:

$$y''(x) = \frac{M_y(x)}{EI} \qquad (6)$$

where $M_y(x)$ is the moment as a function of x, and E is the equivalent module of elasticity, and I is the equivalent moment of inertia of the needle cross section. The equivalent E and I means to consider the module of elasticity and the moment of inertia of the fibers as well (here, we do not consider them since they are small compared to the E and I of the needle). Due to existence of the axial force at the tip of the cantilever beam, it should be analyzed as a beam-column not as a beam. This means that the moment caused by the $F(x)$ should be taken into account, as well:

$$M_y(x) = R_y x + F_x y(x) - M_R, \qquad 0 \le x \le a \qquad (7)$$

$$M_y(x) = M_R - F_x y(x) - R_y x + \frac{w(x-a)^2}{2}, \quad a \le x \le L$$

where R_y and M_R are the reaction force (in y direction) and moment at the support, respectively. The solution of this differential equation is as follows:

$$y^{actual}(x) = \qquad (8)$$

$$\begin{cases} A_1 \cos(\lambda x) + B_1 \sin(\lambda x) + \overbrace{C_1 x + D_1}^{particular\ sol}, & 0 \le x \le a \\ A_2 \cos(\lambda x) + B_2 \sin(\lambda x) + \underbrace{C_2 x^2 + D_2 x + E_2}_{particular\ sol}, & a \le x \le L \end{cases}$$

where $\lambda^2 = F_x/EI$. To find these 9 constant coefficients, we use the following 6 boundary conditions plus plugging the particular solutions into the differential equation (6):

$$y(0) = y'(0) = y''(L) = 0$$
$$y(a^-) = y(a^+),$$
$$y'(a^-) = y'(a^+) \qquad (9)$$
$$y''(a^-) = y''(a^+)$$

It should be noted that all of A_1, B_1, ..., E_2 are functions of $y(L)$. After finding A_2, B_2, ..., E_2, we put $x = L$ into (8) and

solve for $y(L)$. In fact, $y(L)$ is the last parameter we find. The procedure of finding A_1, B_1, ..., D_2, E_2 and $y(L)$ is very cumbersome and was omitted for brevity. In order to find y^{app}, we use equation (4). For the optimization, the second derivatives in (4) are found from the mathematical model we just derived (i.e. (8)). Having y^{actual} and y^{app}, error can be found and optimized against x_1, x_2, and x_3.

B. Finding proper locations

Having a model, we change all model parameters, i.e. a, L, F_x, F_y, and w for any x_1, x_2, and x_3 and find locations that give us the minimum approximation error among all. Since insertion depth is varying in bevel-tip needle steering, following scenarios are possible:

Case 1: no sensor is activated (insertion depth is very low);
Case 2: only one sensor is activated;
Case 3: only two sensors are activated;
Case 4: all three sensors are activated.

The following assumptions were made during optimization: 1) the range of variation for F_x, F_y, and w will be such that the tip deflection does not go beyond 10% of the instantaneous length of the needle. 2) Since the error increases with insertion depth, optimization was performed at the largest insertion depth for each case. Table I shows the parameters we chose for optimization.

TABLE I. PARAMETERS USED FOR OPTIMIZATION

F_x (N)	F_y (N)	w (N/m)	L(mm)
0.0 ~ 1.5	-5.0 ~5.0	-50 ~ 50	0~110

We decided the range of change for x_3 (the sensor close to the tip) be the furthest quarter of the entire length (82.5-110 mm) in order to avoid cases with no sensor activated. The range of change for x_1 is the closest quarter of the needle length from the base (0-27.5 mm) because strain values are the highest close to the base. x_2 range of change is therefore middle half of the needle length (27.5-82.5 mm). In the following, we can find the optimal locations for sensors within the suggested ranges.

Case 1: In this case, no sensor is activated due to the very low insertion depth and no tracking information is available. As a result, this situation should be avoided to possible extent. Luckily, prostate outer most point is 20 mm deep from prenieum (see Fig. 4) which means that the third sensor (closest to tip) can be localized within the first 20 mm of the needle. However, it is desired to minimize the depth of insertion without active sensors. We will make a decision on this in the next section.

Case 2: In this case, one out of three sensors is active. For this scenario, a set of 1st order equations is used to describe the estimated deflection polynomial to be compared with the mathematical model. We mentioned earlier that the range of change for x_3 is 82.5 to 110 mm. Yet, we must take into consideration the location of the second sensor x_2 in order to determine x_3 under the maximum insertion depth before the second sensor is activated. As a result, x_2 was selected to be very close to upper acceptable limit at 79 mm. This means that the highest possible depth with only 1 active sensor is 110-79=31 mm (we will further investigate this suggested

value in Case 3 and Case 4). Taking this into account, we calculated and plotted "Error (x_3)" for the highest depth for any model parameters in Table I as shown in Fig. 5.
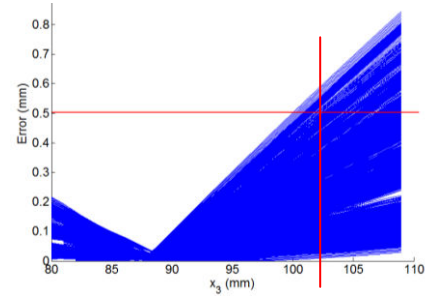

Figure 5. Case 2: maximum error for all force configurations and insertion depths up to 31mm when x_3 is varying.

As seen, an optimal location for one active sensor is 89 mm. However, we choose 99 since it is the closest to the tip yet below 0.5 mm to avoid situation without tip pose information.

Case 3: In this case, two out of three sensors are activated. For this case, a set of 2nd order equations was used to describe the estimated deflection polynomial. Fig. 6 illustrate the 2D projection of the worst error surface as a function of x_2 and x_3 positions for all model parameters. We must take into consideration the location of the third sensor x_3 in order to determine x_2 under the maximum insertion depth before the third sensor is activated. We start with x_1=30 (will further investigate by looking at Case 1 and Case 4). This means the maximum depth with only two sensors activated is 80 mm from the tip. A range of values where the maximum error is below 0.5 mm was determined in Fig. 6.

Case 4: In this case, all sensors are active. A set of 3rd order equations is used to describe the estimated deflection polynomial as shown in (2). Since Error (x_1, x_2, x_3) is a 4D surface, we show its projection onto three planes, x_1-x_2, x_1-x_3, and x_2-x_3 (Fig. 7). The red area shows sensor locations where error is below 0.5 mm for all insertion depth and force configurations.
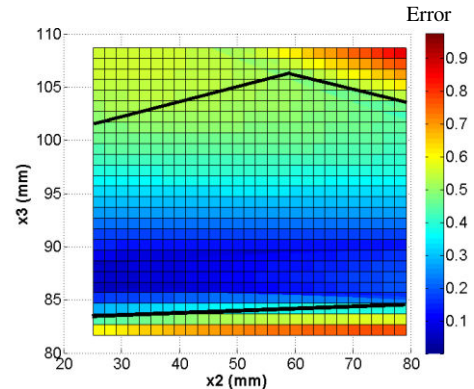

Figure 6. Case 2: maximum error for all model force configurations and depths from 31-79 mm when x_2 and x_3 vary. The safe area is marked between two solid black lines.

Summary: From Case 1, $x_3 = 99$ was the optimum location. The suggested value for x_2 was 79. Fig. 6 and Fig. 7-a, and Fig. 7-c confirm that this suggested value is within the safe region. The suggested value for x_1 was 30. Fig. 7-a , Fig. 7-b

confirm that this value is within the safe region. Table II shows the sensor locations.

TABLE II. OPTIMUM SENSOR LOCATIONS

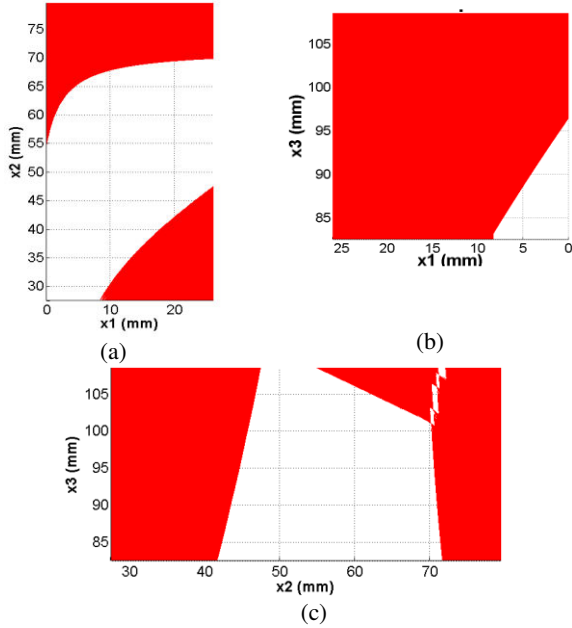| Sensor location	x_1	x_2	x_3
(mm)	30	79	99

(a)   (b)

(c)

Figure 7. Case 4: error for all force configurations and insertion depth above 79 mm when x_1, x_2, and x_3 are varying. Red area shows error below 0.5mm.

After finding the sensor locations, we double check to see whether the error remains below 0.5 mm for all force configurations. In Fig. 8, we plot the worst case error as a function of insertion depth for all force configurations when x_1, x_2, and x_3 are chosen as specified in Table II. As shown, the error increases as insertion depth increases. It drops whenever another sensor is activated. The error remains bellow 0.5 mm for any insertion depth below 100 mm which is the deepest possible target.
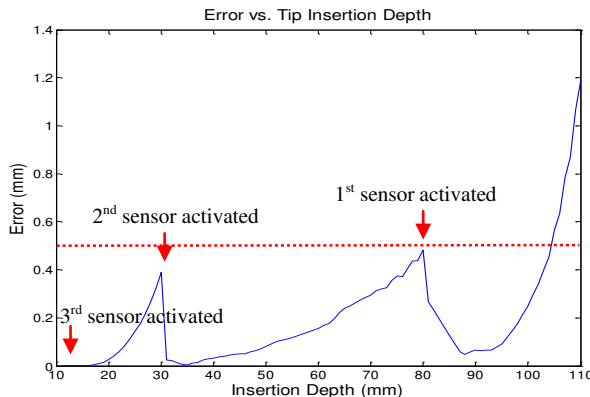

Figure 8. Maximum possible error in tip approximation for any load configuration as a function of insertion depth for the sensor locations specified in Table II.

V. FABRICATION

FBGs with 3 sensors at certain locations were custom made by Technica SA (Beijing, China). The sensors were 5 mm

long, reflectivity >70%, glass fiber, polyimide recoat, and the bandwidth is 0.35-0.45 nm. The wavelengths were constructed at 1540, 1550, 1560 nm (+/-0.5nm) for x_1, x_2, and x_3 respectively. The fibers were 125 um and 5 m long. The accuracy of sensor placement was ±0.5mm.

The inner stylet was a 0.6 mm Titanium 6AL 4V Eli annealed (http://www.amazonsupply.com/) wire with three grooves manufactured 170 mm along the length. The length of the inner stylet was 235 mm. The outer tube was obtained from a 20G × 20 cm MRI biopsy needle (Cook Inc, IN, USA).

A jig was manufactured to carry out lateral milling of the stylet. Fig. 9-a shows such a setup. Two stainless steel plates were overlaid and a channel of 0.6 mm diameter was machined at the corner of the interface between the plates. The channel is 235 mm long and is used to hold the stylet to be machined. Once the needle is placed in the channel and the two plates are bolted together, a brass coin is attached along the stylet length that extends out of the plates. This coin is marked so that it points exact 120-degree rotations for cutting the three channels.

The fibers were glued to the inner stylet channels under microscope with instant adhesive Loctite 415 (Locite Corp., CT, USA). The inner stylet was then passed through the outer tube. The 20G outer tube (175 mm long) was extended by another MRI-compatible 18G needle outer tube to increase the entire needle length to 235 mm. At the end, the handles were glued to the needle. Shrink tube was used to robustly attach the fibers to the needle. Fig. 9-b shows the needle prototype.
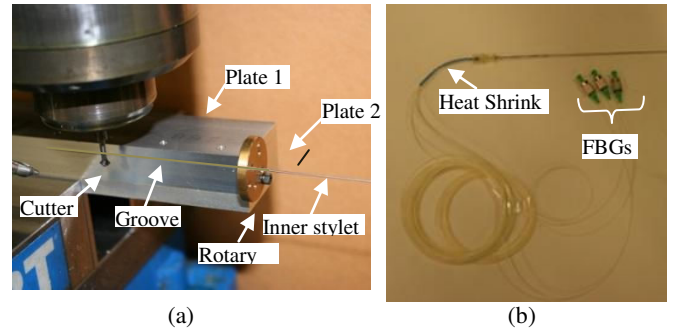

(a)   (b)

Figure 9. (a) Jigs and milling machine for making three grooves along the 0.6 mm needle at 120 degree configuration, (b) Needle prototype.

VI. CALIBRATION

In order to find strain values from wavelength shifts, calibration is required. At each location (i.e. x_1, x_2, and x_3), there are three sensors at 120 degrees. These three sensors together give us ε_{xy} and ε_{xz} in that location. A calibration matrix is therefore defined at each x_i to link the wavelength shifts and strains as follows:

$$\overbrace{\begin{bmatrix} \Delta\lambda_1 \\ \Delta\lambda_2 \\ \Delta\lambda_3 \end{bmatrix}_i}^{\Delta\Lambda} = \begin{bmatrix} c_{xy,1} & c_{xz,1} \\ c_{xy,2} & c_{xz,2} \\ c_{xy,3} & c_{xz,3} \end{bmatrix}_i \overbrace{\begin{bmatrix} \varepsilon_{xy} \\ \varepsilon_{xz} \end{bmatrix}_i}^{\Delta E} \tag{10}$$

where $i = \{1,2,3\}$. These calibration matrices neither depend on the shape of the needle nor the load configuration applied to it. For this reason, we find these matrices for the basic load configuration when a concentrated force at the tip is applied

at the maximum length of the needle (110 mm). $c_{xy,j}$ are found when the needle is deflected in xy plane (i.e. when $\varepsilon_{xz} = 0$) while $c_{xy,j}$ are found when the needle deflects in xz plane (i.e. when $\varepsilon_{xy} = 0$) and $j=\{1,2,3\}$. From linear beam theory for concentrated lateral load at the tip of a cantilever beam ((1) and (6)), one has:

$$y''(x) = \frac{\varepsilon_{xy}(x)}{r} = \frac{F_y x}{EI} \tag{11}$$

and

$$F_y = \frac{3EI y(L)}{L^3} \tag{12}$$

where F_y is the lateral load. From these equations, the strain as a function of x is derived:

$$\varepsilon_{xy}(x_i) = \frac{3r y(L) x_i}{L^3} \tag{13}$$

r is the distance between the central axis of the fiber and the needle axis. This means we only need to measure $y(L)$ in order to find $\varepsilon_{xy}(x_i)$. In order to have a calibration matrix which represents the entire range of needle deflection, we apply different deflections $y(L) = 1, 2, 3, …, 10$ mm once in xy, and once in xz using the experimental setup shown in Fig. 10 as discussed in the follows:
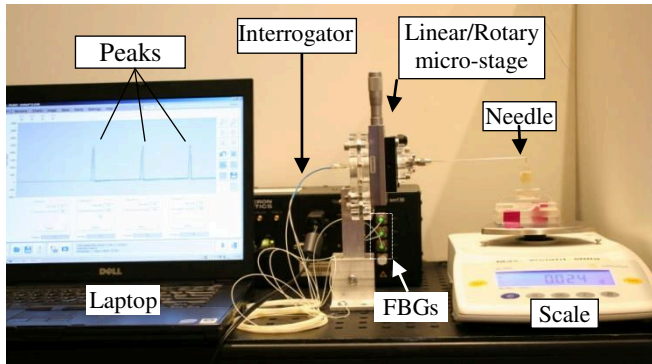

Figure 10. Calibration and experimental setup.

The needle is hold by a pin vice at the center of a 2-DOF micro-stage. The stage can translate vertically with 10 micron resolution thus enabling needle-tip deflection with high accuracy. The rotary stage with 1 degree resolution made it possible to deflect the needle in different planes. In order to detect the first moment of starting deflection, a scale with 0.001gram resolution was used. A sharp blade was placed on top of the scale to enable point contact between the scale and the needle. The micro-stage and the scale were firmly bolted to an anti-vibration table. The interrogator was a 4 channel Micron Optics sm130 (Atlanta, GA, USA), with sampling rate of 2 KHz. The spectrum range is from 1525 nm-1565 nm. Each channel handles one fiber with many sensors (3 sensors in our case). We collected and analyzed data in MATLAB 7.

Now that ε_{xy} and $\Delta\lambda_j$ are found separately, $c_{xy,j}$ is found by fitting the best line to the graph of $\Delta\lambda_j$ vs. $\varepsilon_{xy,j}$ using least square method and find the slope as $c_{xy,j}$. In order to eliminate the effect of temperature change, we subtract $\Delta\lambda_{mean}$ at each x_i from sensor readings. We did temperature compensation during real-time data collection, as well. The results are provided below:

$$C_1 = \begin{bmatrix} 1127.05 & 315.79 \\ -544.97 & -1111.77 \\ -582.08 & 795.97 \end{bmatrix}, \quad C_2 = \begin{bmatrix} 1145.81 & 302.09 \\ -605.81 & -1150.97 \\ -540.00 & 848.88 \end{bmatrix},$$

$$C_3 = \begin{bmatrix} 1234.71 & 466.98 \\ -593.17 & -1283.92 \\ -641.54 & 816.93 \end{bmatrix}.$$

After calibration matrices are found, strains could be calculated as following:

$$\Delta E = C_i^+ \Delta\Lambda \tag{14}$$

C_i^+ is the pseudo-inverse of C_i.

VII. PRELIMINARY VERIFICATION

In order to evaluate accuracy in tip tracking for different insertion depths, we chose maximum insertion depth for each case (worst scenario), applied known deflections to the tip in xy and xz planes (using the setup shown in Fig. 10), and compared them with the estimated value.

One sensor active: The purpose of this experiment was to evaluate needle-tip tracking when only one sensor is active, i.e. when depth < 31 mm. The needle length-of-interest was 27 mm once in xy plane and once in xz plane. The tip was deflected with the micro-stage from 0 up to 3 mm (10 percent of the depth) once forward (loading) and once backward (unloading). The results of 0 degree are shown in Fig. 11-a and the results for 90 degree are shown in Fig. 11-b.

Two sensor active: The purpose of this experiment is to evaluate needle-tip tracking when two out of three sensors are active, i.e. when 31< depth < 80 mm. The needle was placed at the very end of the range at 75 mm outside the vice. The tip was deflected with the micro-stage from 0 up to 7.5 mm (10 percent of the depth) once forward (loading) and once backward (unloading). The results of 0 degree are shown in Fig. 11-c and the results for 90 degree are shown in Fig. 11-d.

Three sensor active: The purpose of this experiment is to evaluate needle-tip tracking when all of three sensors are active, i.e. when depth > 80 mm. The needle was placed at the very end of the range at 110 mm outside the vice. The tip was deflected with the micro-stage from 0 up to 10 mm once forward (loading) and once backward (unloading). The results of 0 degree are shown in Fig. 11-e, the results for 90 degree are shown in Fig. 11-f.
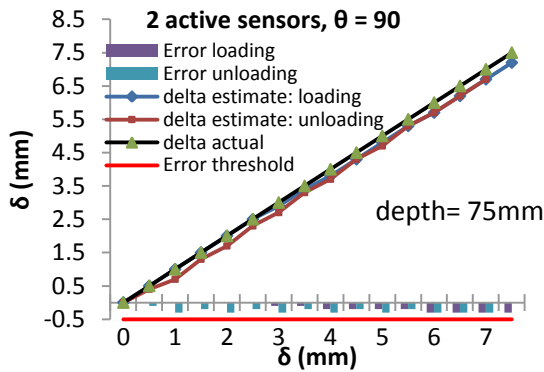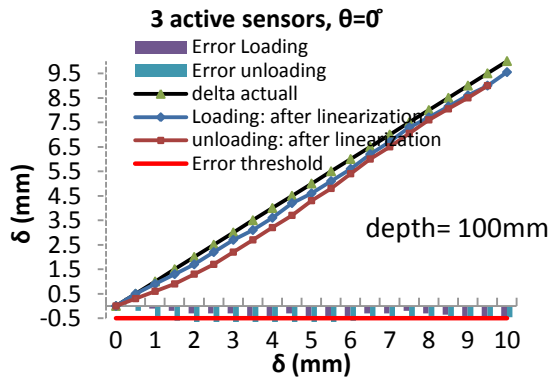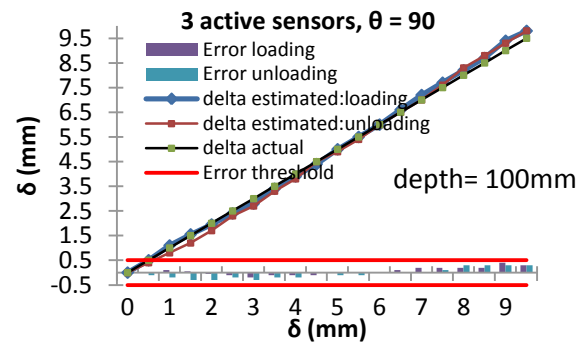

(a)
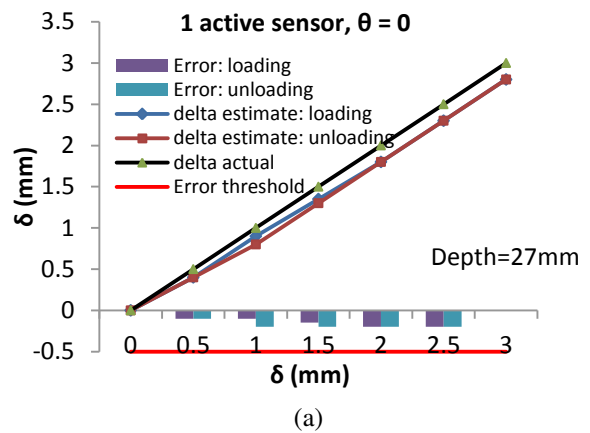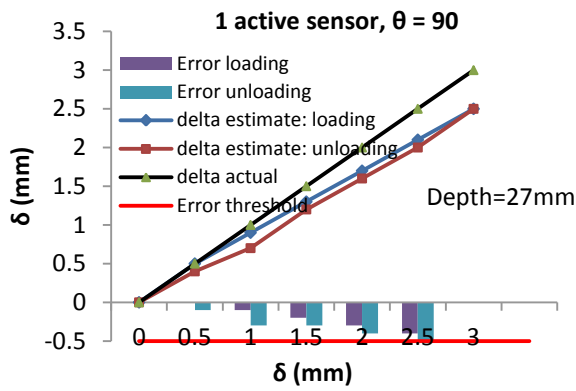
(b)
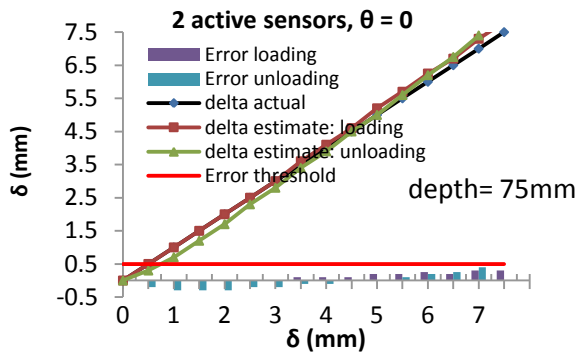
(c)

(d)

(e)

(f)

Figure 11. Experimental results for needle tip position estimation for different depths and needle orientations. (a), (b) one sensor active, (c), (d) two sensor active, (e), (f) three sensors active.

The preliminary results confirmed below 0.5 mm accuracy in needle-tip estimation for almost all insertion depths. Only for the case (e), few times, the error goes slightly above the threshold. The error variation was quite consistent in the repeated tests. Therefore, we could compensate for the error by curve fitting. Nevertheless, the insertion depth of 100 mm is less likely since most of targets are 60-90 mm deep from perineum. Further experiments have been reported in [16].

VIII. REAL-TIME VISUALIZATION IN 3D SLICER

For targeting purposes, prostate anatomy is acquired from the intraoperative MRI such that physician can specify target locations within prostate capsule. In this study, our goal is to overlay 3D shape of the needle on the prostate anatomy in real-time. This feature helps physicians to precisely track needle shape and tip on the fly in order to compensate for any deviation of the tip from target.
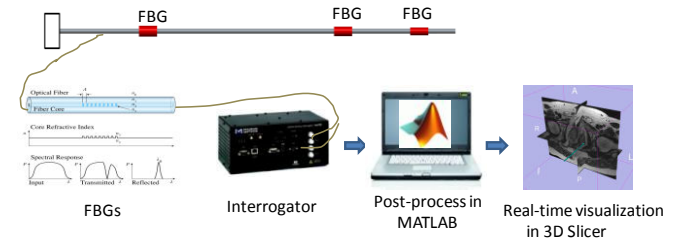

Figure 12. Data flow from FBGs to 3D Slicer.

Fig. 12 shows the data flow from the FBGs until the needle shape is visualized in Slicer. Wavelength shifts are measured by interrogator and sent to MATLAB for post process. Needle profile estimation is done in MATLAB as explained before. In order to send the 3D shape profile of the needle from MATLAB to Slicer, we used OpenIGTLink (http://openigtlink.org/). In our application, it provides communication between Slicer and MATLAB. Since OpenIGTLink is written in C++, MEX files were necessary to make possible calling OpenIGTLink commands in MATLAB that have recently been developed [17]. In Slicer, the needle was visualized as a group of fiducials placed next to each other. Fig. 13 shows a visualization software when needle is deflected with two inflection points.
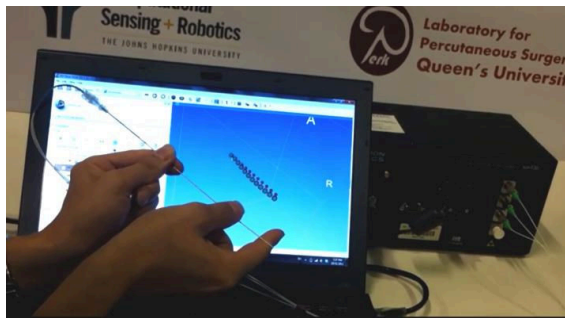
Fig.ure 13. Real-time 3D shape tracking of a 20G x 110 mm needle in 3D Slicer: 2 inflection points experiment. To see movie, click here.

A video is also provided to show the functionality of the proposed system in real-time 3D shape tracking of the needle.

IX. CONCLUSIONS AND FUTURE WORKS

This study presented development of one of the key technologies for teleoperated bevel-tip needle steering under real-time MRI guidance i.e. 3D tracking of the needle tip with better than 0.5 mm accuracy and higher bandwidth than continuous MRI imaging. Results showed needle tip tracking error below 0.5 mm for all insertion depths, covering all clinically relevant insertion depths in transperineal prostate needle placement procedures. Real-time 3D shape of the needle was overlaid on the intraoperative prostate MRI image using 3D Slicer. This technology has been incorporated to the master-slave system and will be used for patient study in the near future.

REFERENCES

[1] R. Seifabadi, I. Iordachita and G. Fichtinger, "Design of a teleoperated needle steering system for MRI-guided prostate interventions," in *Biomedical Robotics and Biomechatronics (BioRob), 2012 4th IEEE RAS & EMBS International Conference on,* 2012, pp. 793-798.

[2] V. Lagerburg, M. A. Moerland, J. J. Lagendijk and J. J. Battermann, "Measurement of prostate rotation during insertion of needles for brachytherapy," Radiotherapy and Oncology, vol. 77, pp. 318-323, 2005.

[3] R. Seifabadi, N. B. Cho, S. E. Song, J. Tokuda, N. Hata, C. M. Tempany, G. Fichtinger, and I. Iordachita,. Accuracy Study of a MRI-guided Robotic System for Prostate Needle placement. *The International Journal of Medical Robotics and Computer Assisted Surgery*, Published online June 2012, DOI: 10.1002/rcs.1440

[4] G. S. Fischer, and H. Su, "apparatus and methods for MRI-compatible haptic interface," *U.S. Patent* No. 20,120,265,051, 2012.

[5] R. Monfaredi, R. Seifabadi, G. Fichtinger, and I. Iordachita, "Design of a decoupled MRI-compatible force sensor for robot-assisted prostate interventions," in *Proc. SPIE Medical Imaging, In press, 2013*.

[6] M. Ries, B. D. de Senneville, S. Roujol, Y. Berber, B. Quesson and C. Moonen, "Real - time 3D target tracking in MRI guided focused ultrasound ablations in moving tissues," *Magnetic Resonance in Medicine,* vol. 64, pp. 1704-1712, 2010.

[7] S. E. Song, N. B. Cho, I. I. Iordachita, P. Guion, G. Fichtinger and L. L. Whitcomb, "A study of needle image artifact localization in confirmation imaging of MRI-guided robotic prostate biopsy," in *Robotics and Automation (ICRA), 2011 IEEE International Conference on,* 2011, pp. 4834-4839.

[8] K. O. Hill, and G. Meltz, "Fiber Bragg grating technology fundamentals and overview," Journal of Lightwave Technology, 15(8),1263–1276 (1997).

[9] I. Iordachita , Z. Sun, M. Balicki, J. Kang, S. Phee, J. Handa, P. Gehlbach, R.Taylor. A sub-millimetric, 0.25 mn resolution fully integrated fiber-optic force-sensing tool for retinal microsurgery. *International Journal of Computer Assisted Radiology and Surgery (IJCARS)*, vol. 4(4), pp. 383–390.

[10] Y.-L. Park, S. Elayaperumal, B. Daniel, S. C. Ryu, M. Shin, J. Savall, R. J. Black, B. Moslehi, and M. R. Cutkosky. Real-time estimation of 3-D needle shape and deflection for MRI-guided interventions. *IEEE/ASME Trans. Mechatron.*, vol. 15, no. 6, pp. 906–915, Dec. 2010.

[11] ENDOSENSE. Medical apparatus system having optical fiber load sensing capability, 2006.

[12] L. Zhang, J. Qian, Y. Zhang, and L. Shen. On SDM/WDM FBG sensor net for shape detection of endoscope. in *Robotics and Automation (ICRA), 2005 IEEE International Conference*, 4:1986–1991, 2005.

[13] J. Tokuda, G. Fischer, C. Csoma, S. DiMaio, D. Gobbi, G. Fichtinger, C. Tempany and N. Hata, "Software strategy for robotic transperineal prostate therapy in closed-bore MRI," *Medical Image Computing and Computer-Assisted Intervention–MICCAI 2008,* pp. 701-709, 2008.

[14] H. Xu, A. Lasso, S. Vikal, P. Guion, A. Krieger, A. Kaushal, L. Whitcomb, and G. Fichtinger (2010). Accuracy validation for MRI-guided robotic prostate biopsy. *SPIE Medical Imaging: Visualization, Image-Guided Procedure, and Modeling*, 7625, 762517-762517.

[15] S. P. Timoshenko, "History of strength of materials". *Dover publications*, 1983.

[16] R. Seifabadi, "Teleoperated MRI-guided Prostate Needle Placement", PhD thesis, Department of Mechanical Engineering, Queen's University, Canada, 2013.

[17] http://www.na-mic.org/Wiki/index.php/OpenIGTLink/Matlab

[18] R. Seifabadi, S. E. Song, A. Krieger, N. B. Cho, J. Tokuda, G. Fichtinger and I. Iordachita, "Robotic system for MRI-guided prostate biopsy: feasibility of teleoperated needle insertion and ex vivo phantom study," International Journal of Computer Assisted Radiology and Surgery, vol. 7, pp. 181-190, 2012